Supporting Information

Production of $Ni(OH)_2$ Nanosheets by Liquid Phase Exfoliation: High Performance Oxygen Evolution Catalysts and Supercapacitor Electrodes

Andrew Harvey,[1,2^] Xiaoyun He,[1,2^] Ian J. Godwin,[1,2] Claudia Backes,[1,2] David McAteer,[1,2] Nina C. Berner,[1,3] Niall McEvoy,[1,3] Auren Ferguson,[1,2] Aleksey Shmeliov,[1,3] Michael E. G. Lyons,[1,3] Valeria Nicolosi,[1,3] Georg S. Duesberg,[1,3] John F Donegan[1,2] and Jonathan N. Coleman[1,2]*

[1]*CRANN & AMBER, Trinity College Dublin, Dublin 2, Ireland*

[2]*School of Physics, Trinity College Dublin, Dublin 2, Ireland*

[3]*School of Chemistry, Trinity College Dublin, Dublin 2, Ireland*

*colemaj@tcd.ie

^ These authors contributed equally

Content

1. Supporting methods

X-ray powder diffraction

The structure and phase analyses were performed using X-ray diffraction (XRD) with Cu Kα1 radiation (Se X-ray diffractometer in a Bragg–Brentano configuration). The detected diffraction angle (2θ) was scanned from 10° to 80° with a scan speed of 0.002° s^{-1} (see section 2 for results).

IGC Experimental Description:

IGC experiments were carried out on a Surface energy analyser (SEA) from Surface Measurement Systems, UK. Helium and methane (BOC research grade) were used as the carrier and dead time gas respectfully. The dispersive probes; nonane, octane, heptane and hexane were used to measure the dispersive surface energy and specific probes; dichloromethane, ethyl acetate, 1-propanol, ethanol, methanol were used to measure the specific surface energy. 16mg of $Ni(OH)_2$ powder was packed into a 2mm glass column and plugged at each end using salinised glass wool. The experiments were conducted at 343K with a carrier gas flow rate of 10 mL/min.

Choice of surfactant

Different surfactants were screened regarding their ability to stabilise liquid-exfoliated $Ni(OH)_2$. Notably, these were sodium cholate (main manuscript), sodium dodecyl benzene sulfonate (SDBS, Sigma Aldrich, item no. 289957) and the non-ionic surfactant Brij (Sigma Aldrich, item no. 16005). For the surfactant screening, 10$mgml^{-1}$ of pretreated $Ni(OH)_2$ powder was sonicated in 50 mL of surfactant solution for 1 hour and was centrifuged for 120mins at 1.5krpm. The critical micelle concentrations were chosen as surfactant concentration in each case (SC: 6 g/L, SDBS 1 g/L, Brij 0.1 g/L). The supernatant was decanted and the absorption and extinction were measured in a 4mm path length cuvette using a PerkinElmer Lambda 650 spectrometer (see section 3 for results).

IR spectroscopy

DRIFT-IR spectra were acquired using a Perkin Elmer Frontier spectrometer equipped with a diffuse reflectance unit. Samples were prepared by grinding the respective powders obtained after vacuum filtration in a CsI (Sigma Aldrich, 99.9 % purity) matrix. The CsI baseline was subtracted from the spectra. All spectra were baseline corrected after acquisition (see section 4 for results).

2. Characterisation of bulk and pretreated $Ni(OH)_2$ (XRD and XPS)

XRD and XPS was performed on the bulk pretreated powder to gain insights on the purity of the powder as well as the to determine the phase of the material, *i.e.* whether it was in the α- or β- phase. In both cases the powder was mixed in water (*i.e.* simply by shaking) and vacuum filtrated onto nitrocellulose membranes and dried in air.

As can be seen in both the XRD spectra (Fig S1) and the XPS spectra (Fig S2) are identical thus showing that there is no phase change in the pretreatment step and that the original powder was largely free of contaminates. In both cases the powders are >99% $Ni(OH)_2$ as confirmed by XPS. We note that we observe adsorbed nitrate in both Raman and IR spectra (see below). However, no nitrogen is detected in the XPS survey spectra suggesting that these adsorbates are commonly observed residual impurities from the synthesis trapped between the layers. Since XPS is highly surface sensitive, they cannot easily be detected. In addition, N in general has a low XPS cross section making it more difficult to detect

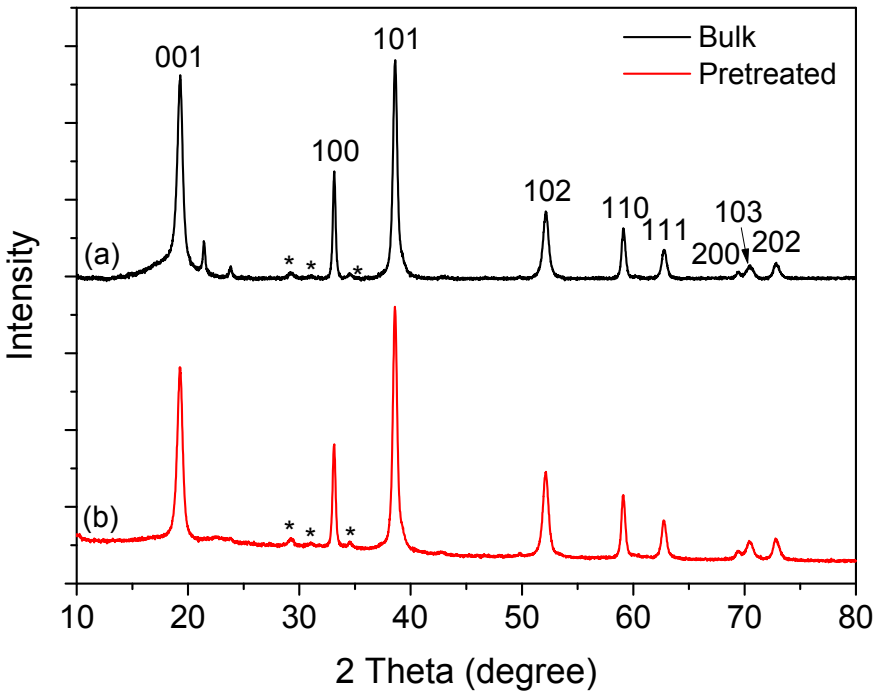

Figure S1) XRD spectra of as-received and pretreated $Ni(OH)_2$ exhibiting clear characteristics of the single phase β-$Ni(OH)_2$ with a suitably crystalline hexagonal structure (a = 0.3126 nm, c = 0.4605 nm)[1]. No peaks from other phases are found, suggesting high purity of the as-received β-$Ni(OH)_2$[2, 3].

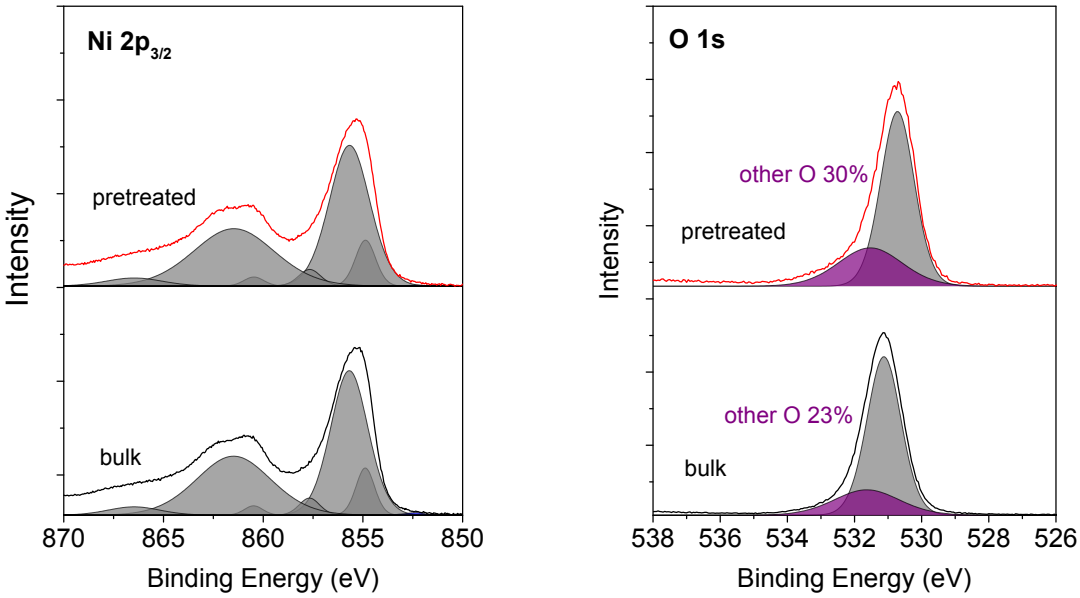

Figure S2) XPS core level spectra A) Ni $2P_{3/2}$. B) O 1s) of both bulk and pretreated $Ni(OH)_2$ powder. The Ni $2P_{3/2}$ spectra are virtually identical and consistent with >99% $Ni(OH)_2$ showing contributions from no other nickel species than Ni^{2+}. No other trace elements were detected in the survey spectra.

3. Measurement of Surface energy By IGC

Inverse gas chromatography (IGC) is a well-established method for measuring the surface energy of heterogeneous solids.[4-6] IGC is a gas sorption technique that operates by injecting different kinds of probe solvents into a column containing the sample and measuring the time taken for them to elute through it. The elution time is converted to retention volume (V_N) which can be used to measure both the dispersive surface energy (γ_d)[7-9] and the surface energy due to specific interactions ($\gamma_{specific}$) [10, 11] of a material where the total surface energy (γ_T) is the sum of the components.[12] Surface energy profiles which map the surface energy of a sample as a function of surface coverage (ϕ) by carefully controlling the amount of probe injected into the column[12, 13] are used here to measure the surface energy associated with the basal plane of $Ni(OH)_2$.

The Dorris-Gray method was used to measure γ_d [14] for ϕ ranging from 0.02-0.25 by measuring the free energy of adsorption ($RTLnV_N$) of a series of n-alkane probes as a function of their carbon number, n, as shown in figure xA. The slope of the fitted line in figure xA is used to calculate γ_d for one value of ϕ. This is repeated for each ϕ to get the γ_d profile of $Ni(OH)_2$ as shown in figure xB. γ_d profiles give a range of values depending on coverage. At low coverage, γ_d is due to high energy sites on the sample surface such as defects[15, 16] and γ_d at high coverage is lower in energy and is attributed to the basal plane of material. The basal plane surface energy is equivalent to the surface energy often quoted from solubility studies using liquid exfoliation.[17] Surface energy profiles can be fitted to an empirical exponential decay function allowing the extrapolation of the surface at full coverage, $\gamma_{d,\phi=1}$,[5, 18] as shown in figure xB. From this, $\gamma_{d,\phi=1}$ for $Ni(OH)_2$ was found to be 61 mJ/m^2.

The specific free energy of adsorption ($\Delta G_{specific}$) of $Ni(OH)_2$ was measured for 5 specific probes using the polarisation method[10] . The polarisation method allows both dispersive and specific probes to be represented on the same scale, allowing $\Delta G_{specific}$ to be calculated by

taking the difference in $RTLnV_N$ between the specific probe and the alkane reference line as shown in figure xC , this is done to remove any dispersive contribution to $\Delta G_{specific}$. This procedure was repeated for each value of ϕ to produce $\Delta G_{specific}$ profiles for each specific probe, which are shown in figure xD. The $\Delta G_{specific}$ profiles have the same general shape as the γ_d profiles but are presented in units of kJ/mol. 1-propanol, ethanol and methanol have approximately double the $\Delta G_{specific}$ than dichloromethane and ethyl acetate at high ϕ which indicates the presence of hydrogen bonding between these probes and $Ni(OH)_2$. Unfortunately, there is no direct method to harmonise these units for the alcohols but we can measure the polar (acid-base) surface energy (γ_p) of $Ni(OH)_2$ using the mono-polar probes (dichloromethane and ethyl acetate) by the van Oss-Good method[19] with the Della-Volpe scale[20] as shown in figure xE. This method calculates γ_p by taking the geometric mean of the acid parameter of γ_p (from dichloromethane) and the base parameter of γ_p (from ethyl acetate). The same exponential fitting as used for γ_d was applied to this to get $\gamma_{p,\phi=1}$ = 4 mJ/m^2. Considering this result with $\Delta G_{specific}$ for the alcohols being twice that of the polar probes, we can crudely estimate the specific surface energy ($\gamma_{specific}$) of $Ni(OH)_2$ to be between 4-9 mJ/m^2 giving γ_T of $Ni(OH)_2$ to be between 65-70 mJ/m^2.

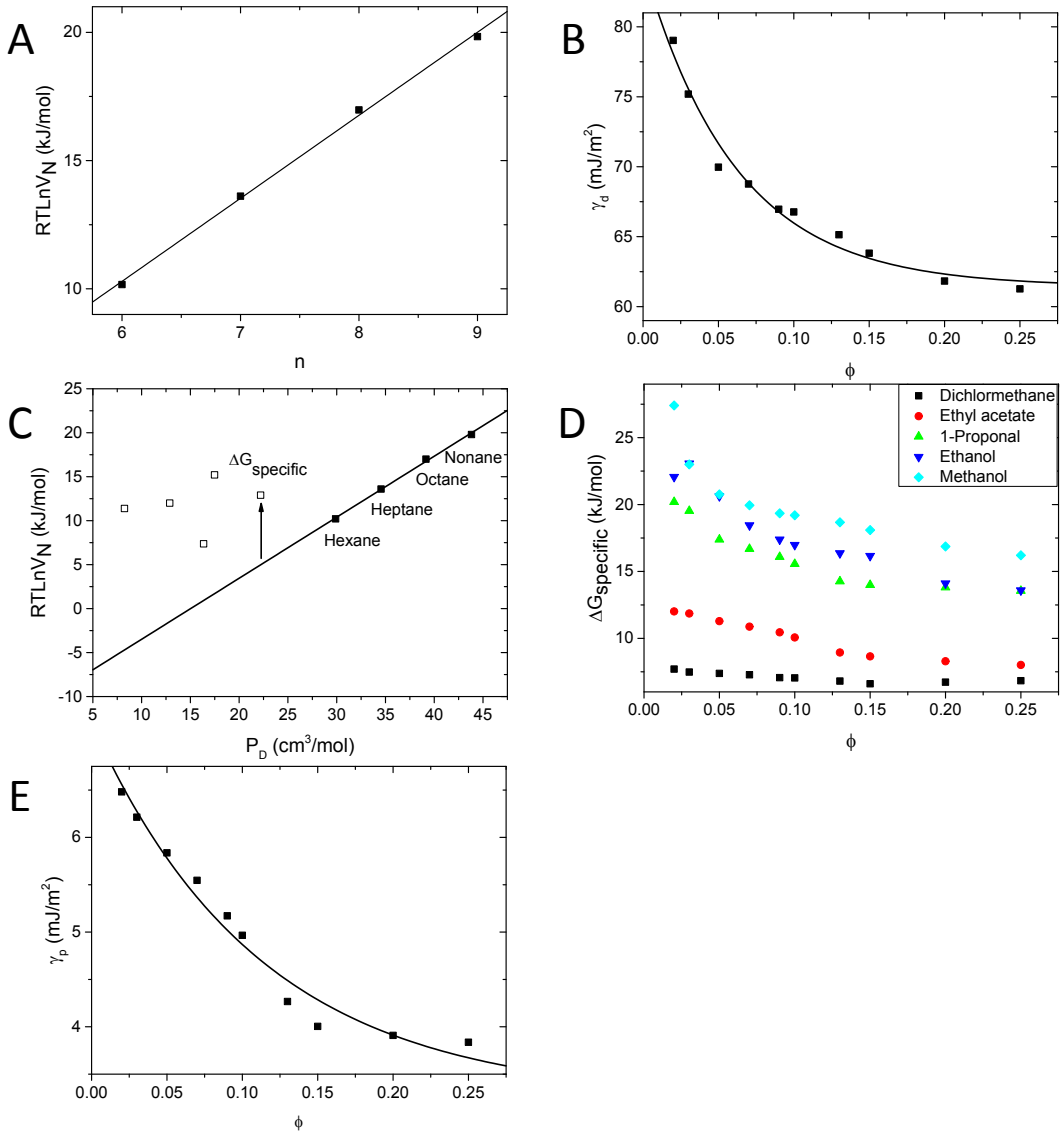

Figure S3: A) Dorris-Gray plot of $Ni(OH)_2$ at 0.25 surface coverage (ϕ) yielding a dispersive surface energy (γ_d) of 61.3 mJ/m^2. B) γ_d profile of $Ni(OH)_2$ with fitted exponential decay function yielding the basal plane (full coverage) surface energy, $\gamma_{d,\phi=1}$ = 61 mJ/m^2. C) Polarisation method for the measurement of the specific free energy of adsorption ($\Delta G_{specific}$) of specific probes at ϕ=0.25. D) $\Delta G_{specific}$ profiles of $Ni(OH)_2$ for the 5 specific probes used. E) Fitted polar surface energy (γ_p) profile of $Ni(OH)_2$ giving $\gamma_{p,\phi=1}$ = 4 mJ/m^2.

4. Optimisation of exfoliation conditions

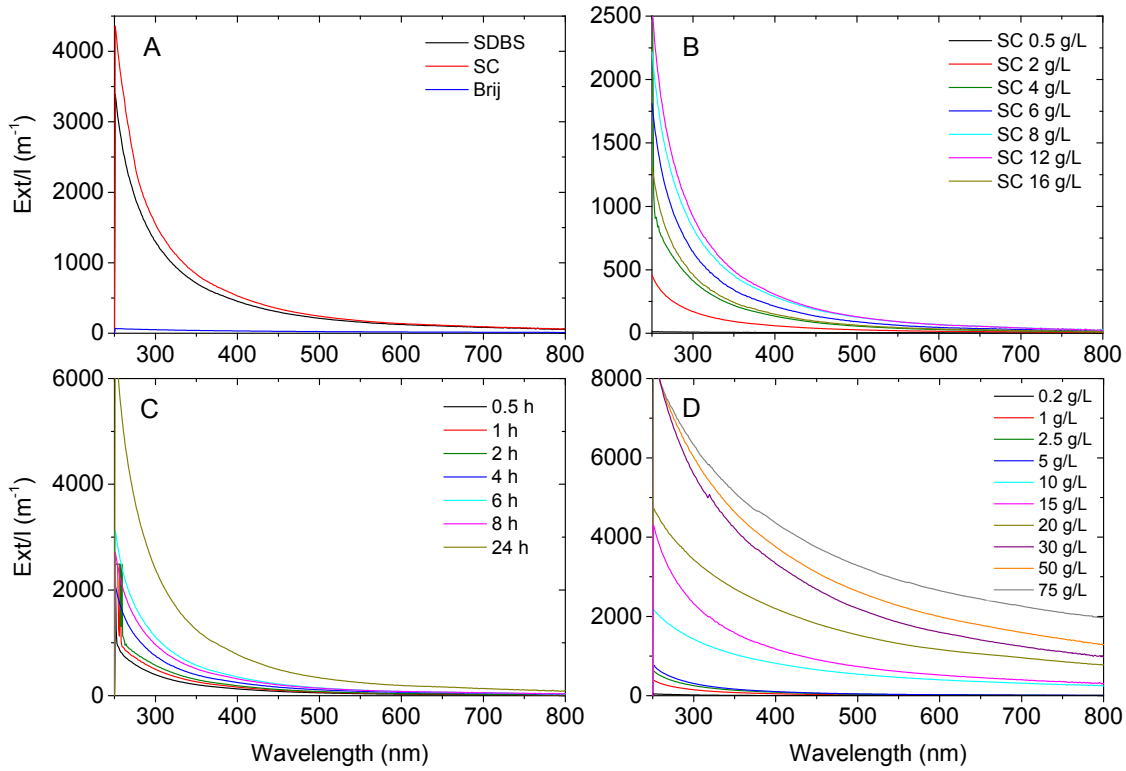

Figure S4 A) *Extinction spectra for differing surfactants sodium dodecylbenzenesulfonate (SDBS), sodium cholate (SC) and Brij,* t_{sonic} *= 1 h,* C_i *= 10g/L,* C_{surf} *= CMC of relevant surfactant. B) Extinction spectra for varying SC concentrations as indicated in the figure legend,* t_{sonic} *= 1 h,* C_i *= 10g/L. C) Extinction spectra as a function of wavelength for varying sonication time,* C_i *= 10g/L,* C_{SC} *= 9g/L. D) Extinction spectra for differing initial* $Ni(OH)_2$ *concentration,* t_{sonic} *= 1 h,* C_{SC} *= 9g/L. In all cases, the supernatant after centrifugation at 1 krpm (2 h) was analysed.*

To ensure that the highest concentrations of exfoliated nanosheets are achieved whilst maintaining dispersions that don't sediment or reaggregate, it is essential to optimise the exfoliation conditions. This was achieved by measuring the dispersed concentration of $Ni(OH)_2$ after varying the surfactant used, surfactant concentration, sonication time and starting powder concentration. The concentration was measured through extinction spectroscopy (Fig S3) using equation 5 from the main ms:

$$C = \frac{Ext_{386nm}}{2312l}\left[\frac{4}{n} - 1\right]^{-0.8} \qquad (5)$$

although similar results were found using the absorption coefficient at 386 bnm: $<\alpha_{386nm}>=14$ $Lg^{-1}m^{-1}$.

Sodium cholate was chosen as standard surfactant, even though it should be noted that the anionic surfactant SDBS also yielded similar concentrations. Interestingly, the non-ionic surfactant Brij was found to be significantly less efficient in stabilising the nanosheets.

Additional low-resolution TEM images of the standard sample are displayed in figure S4 showing a large abundance of nanosheets with varying shapes, sizes and thicknesses.

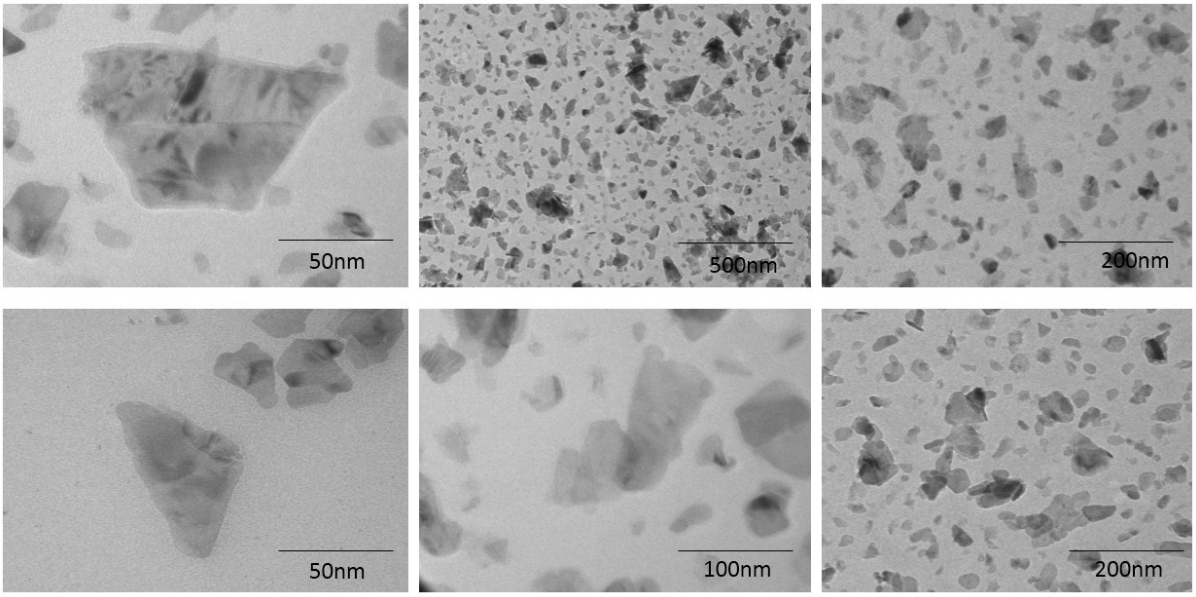

Figure S5) Low res TEM images for the standard $Ni(OH)_2$ dispersion, t_{sonic} = 4 h, C_i = 20g/L, C_{surf} = 9g/L, f=2.5krpm, t_{cf} = 2h.

5. Additional characterisation of exfoliated $Ni(OH)_2$ nanosheets

5.1 AFM Characterisation

Atomic force microscopy (AFM) was carried out on a Dimension ICON3 scanning probe microscope (Bruker AXS S.A.S.) in tapping mode in air under ambient conditions using aluminum coated silicon cantilevers (OTESP-R3). A drop of the dispersion (20 µL) was deposited on a pre-heated (150 °C) Si/SiO_2 wafer (1×1 cm^2) with an oxide layer of 300 nm. The high concentration dispersion was diluted with water immediately prior to deposition to reduce surfactant concentrations to yield a pale colloidal dispersion. After deposition, the wafer was rinsed with ~5 mL of water and ~5 mL of isopropanol. Typical image sizes were 2×2 μm^2 at scan rates of 0.8-1.0 Hz with 512 lines per image (fig S5A-D). The apparent thickness was converted to number of layers, N, using previously developed step-height analysis[21, 22] as shown in the fig S5E. A map of flake area (represented by length times width) is plotted versus thickness in figure S5F. Histograms of nanosheet thickness and length are shown in figure S5G and H.

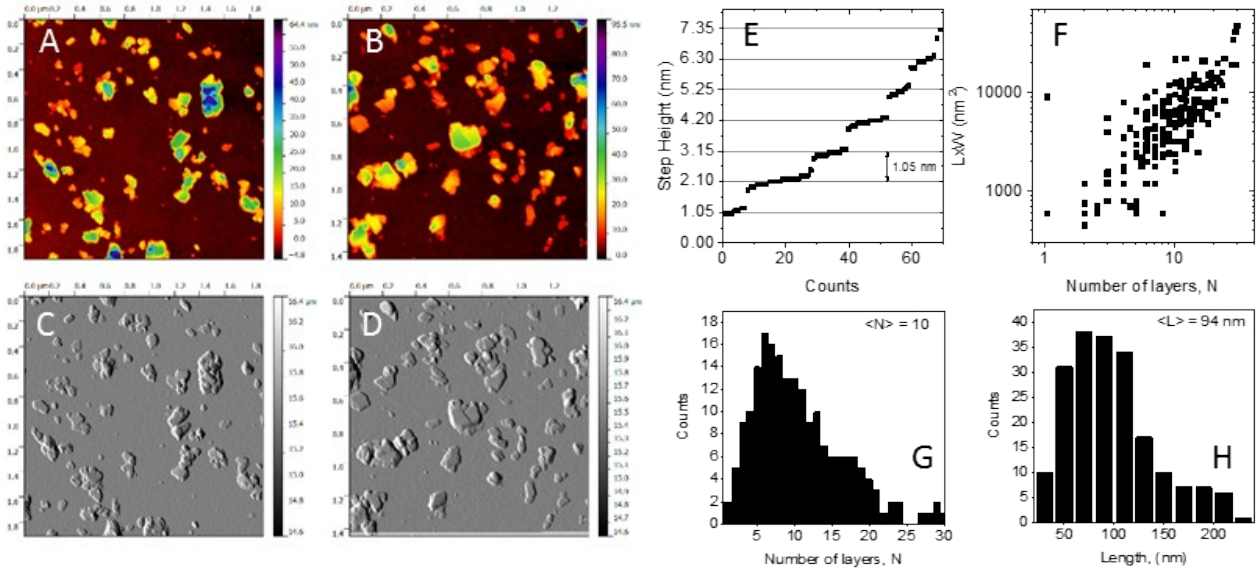

Figure S6: A-D) Typical AFM height (top) and phase (bottom) images. E) Step height analysis [22, 23] showing the apparent height of $Ni(OH)_2$ monolayers to be 1.05 nm. F) Nanosheet area plotted versus thickness. G-H) Histograms of nanosheet thickness and length.

5.2 Raman spectroscopy

As outlined in the main manuscript, the Raman spectra clearly evidence that both bulk and exfoliated material is predominantly β-$Ni(OH)_2$. A more detailed analysis and discussion is presented in the following. The non-baseline corrected spectra (normalised to the maximum) in figure S5A show that the exfoliated β-$Ni(OH)_2$ show an increased, but still weak broad fluorescence background. Such fluorescence background is often observed in $Ni(OH)_2$, even though the reasons remain currently unknown.[24] The spectra in Figures S5B and S5C were baseline-corrected and re-normalised to the maximum to allow for a better comparison. In the low-wavenumber region (Figure S6B), the E_g and A_{1g} lattice vibrations are observed. Furthermore, the much weaker and broader E_g O-H bending mode is discernible at ~880 cm^{-1}.[24] The additional weak vibrations at 740 and 1050 cm^{-1} are attributed to adsorbed nitrate presumably a residual from the synthesis.[24] Figure S5C shows the high wavenumber region of the intense A_{1g} O-H stretching vibration. Both the symmetrical and sharp lineshape, as well as the position at 3585 cm^{-1} are characteristic of the β-phase.[24] Only very faint features from disordered or surface O-H vibrations[24] are observed at higher Raman shift. Importantly, apart from the slight fluorescence background in the case of the exfoliated nanosheets, all three spectra of bulk, pretreated and exfoliated $Ni(OH)_2$ are virtually identical, even in terms of peak intensity ratio. This strongly supports the finding no damage was done during the processing.

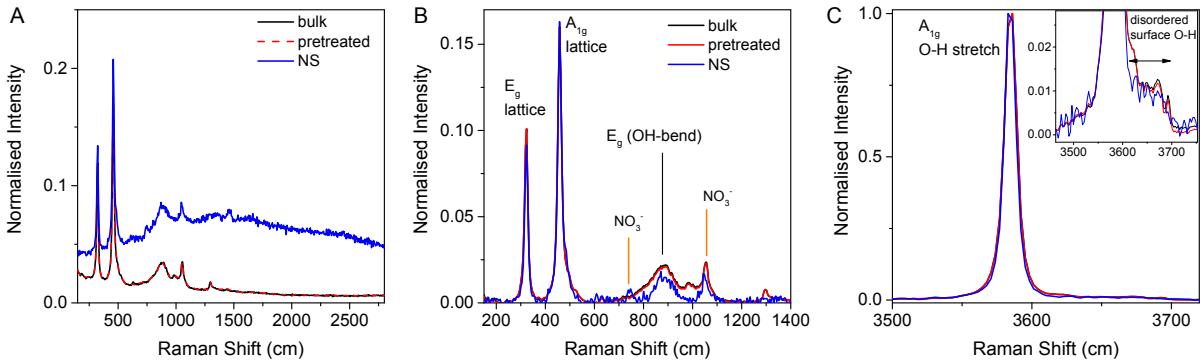

Figure S7: A) Raman spectra normalised to the maximum of bulk $Ni(OH)_2$, pretreated $Ni(OH)_2$ and $Ni(OH)_2$ nanosheets without background subtraction, b) Raman spectra after background subtraction in the low wavenumber region. C)Raman spectra after background subtraction in the high wavenumber region. Inset: zoom in at tail of the O-H stretch-mode.

5.3 IR spectroscopy

To further confirm the phase and composition of the material, samples were subjected to diffuse reflectance infrared fourier transform (DRIFT) spectroscopy in CsI matrix (see supporting methods). The IR spectra are summarised in Figure S6. The as-recorded spectrum of the bulk powder shows the characteristic vibrations of β-$Ni(OH)_2$ as assigned in the figure.[24] In addition, adsorbed water, nitrate and probably hydrocarbons are observed as indicated. In Figure S6B, we directly compare baseline-subtracted and normalised spectra of bulk, pretreated and exfoliated $Ni(OH)_2$. Again, all spectra are very similar further supporting that no damage was introduced by the sonication and processing. In fact, the spectrum of the exfoliated nanosheets shows less adsorbed water, nitrate and hydrocarbons. This indicates that impurities that were trapped between the individual layers are partly released and removed by the exfoliation process. Apart from the aliphatic CH_x stretching vibrations centred at 2930 cm^{-1}, no features from the SC surfactant are observed suggesting that it can be widely removed by washing the filtered films. A spectrum of pure SC is displayed in Figure S6C as comparison.

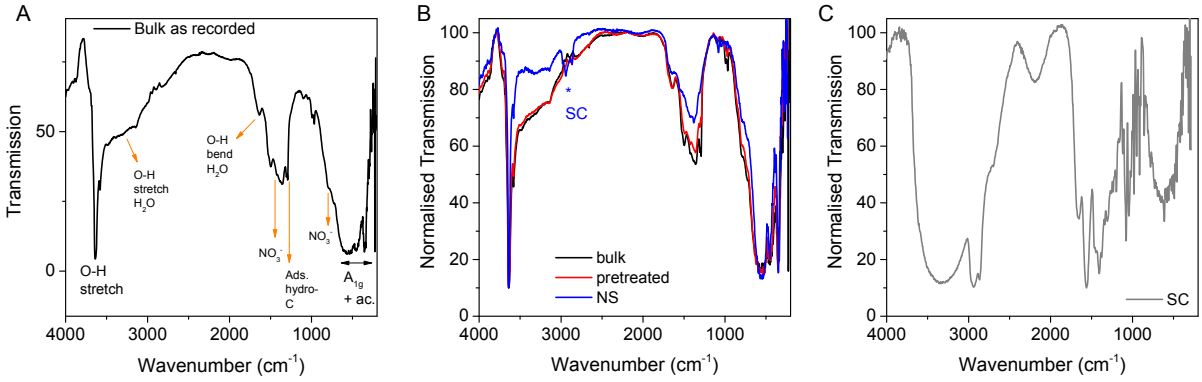

Figure S8: A) As recorded DRIFT spectrum of bulk $Ni(OH)_2$ with modes assigned. The matrix CsI is subtracted from the spectrum. B) Baseline subtracted and normalised DRIFT spectra of bulk $Ni(OH)_2$, pretreated $Ni(OH)_2$ and $Ni(OH)_2$ nanosheets. C) DRIFT spectrum of sodium cholate.

5.4 HRTEM

The electrochemical performance of electrodes based on $Ni(OH)_2$ nanosheets improves significantly under activation. As described in the main text, electrodes were activated by applying a constant current density of 10 mA cm^{-2} for 100 hours. To investigate the effect of activation on nanosheet structure, we preformed high resolution transmission electron

microscopy (HRTEM) on as-produced nanosheets and those which had been activated. To facilitate HRTEM imaging, the nanosheets were exfoliated by sonication in 2-propanol as this tends to reduce imaging problems associated with residual solvent. Pre-treated $Ni(OH)_2$ was sonicated in 2-propanol for 4 hours at a concentration of $20mgml^{-1}$ and then centrifuged at 1.5kRPM for 2 hours. The resulting supernatant was decanted and a few drops were pipetted onto a holey carbon TEM grid. For the post-activation sample, the electrode was sonicated for one hour in a low-power sonic bath to remove the $Ni(OH)_2$ nanosheets from the Ni foam. A few drops of this dispersion were pipetted onto a second TEM grid.

Shown in figure S9A is a typical HRTEM image of an as-prepared few-layer $Ni(OH)_2$ nanosheet. While it is quite challenging to obtain high quality HRTEM images of liquid-exfoliated nanosheets due to the presence of residual solvent, we can gather information about the nanosheet structure by obtaining fast Fourier transforms (FFTs) from selected regions (white boxes). The inset in figure S9A shows an FFT which is typical of those obtained from as-prepared nanosheets. This shows the nanosheet structure to be hexagonal as expected (see figure 1A, main text).

In contrast, figure S9B shows a typical HRTEM image of a few-layer $Ni(OH)_2$ nanosheet that had been activated for 100 hrs. While the activated nanosheets do not look dramatically different from the as-prepared ones, significant differences are observed once FFTs are analysed. A typical FFT for an "after activation" sample is shown as an inset to figure S9B. In general no spots (or in a minority of cases, very poorly-defined spots) are observed indicating the basal planes to be largely amorphous. This is a distinct change from the as-prepared case which generally displayed crystallinity.

There are two possible reasons for this loss of crystallinity. The first possibility is that activation involves a chemical reaction which results in a product which is inherently less crystalline than the starting β-$Ni(OH)_2$. Electrochemically oxidation of β-$Ni(OH)_2$ upon application of a sufficiently anodic potential, is known to result in a transformation to β-NiOOH.[25, 26] While β-$Ni(OH)_2$ has a layered brucite-type crystal structure in a well-defined ABAB stacking arrangement, the charged β-Ni(OOH) state is less well-defined with a broad x-ray diffraction pattern.[27] This material is thought to retain the same brucite type structure but with some additional stacking faults. However, upon prolonged polarisation or 'overcharging' β-Ni(OOH) has been suggested to form γ-Ni(OOH).[28] After activation of our β-$Ni(OH)_2$ sample by such prolonged polarisation, we therefore believe we have β-Ni(OOH) or γ-Ni(OOH) or most likely a mixture of both as the relative amount each oxide present depends

on the relative charge of the system. [29] In addition we could also residual amounts of $Ni(OH)_2$. Such a mixed system would be expected to be quite disordered, consistent with the loss of crystallinity observed by HRTEM. Our results corroborate well with Sac-Epée and co-workers[29] who observed a similar loss in crystallinity when comparing a hydrothermally prepared β-$Ni(OH)_2$ to an oxidised γ -Ni(OOH) sample.

The second possibility is that the activated nanosheets are actually initially crystalline but are more susceptible to beam damage than $Ni(OH)_2$. This could result in amorphous-isation quite rapidly within the microscopy. In a recent publication, Casas-Cabanas and coworkers[26] noted that HRTEM studies on Ni(OOH) has proven difficult to date as it tends to degrade inside electron microscope columns. This degradation was limited however by operating under low-beam irradiation conditions and short-term exposures however some degradation cannot be ruled out.[26]

HRTEM Sample Preparation

Dispersion of $Ni(OH)_2$ nanoparticles in IPA was drop-cast onto Lacey Carbon grid and baked out overnight at 100°C in vacuum oven. Imaging was performed with an FEI Titan transmission electron microscope operated at 300 keV.

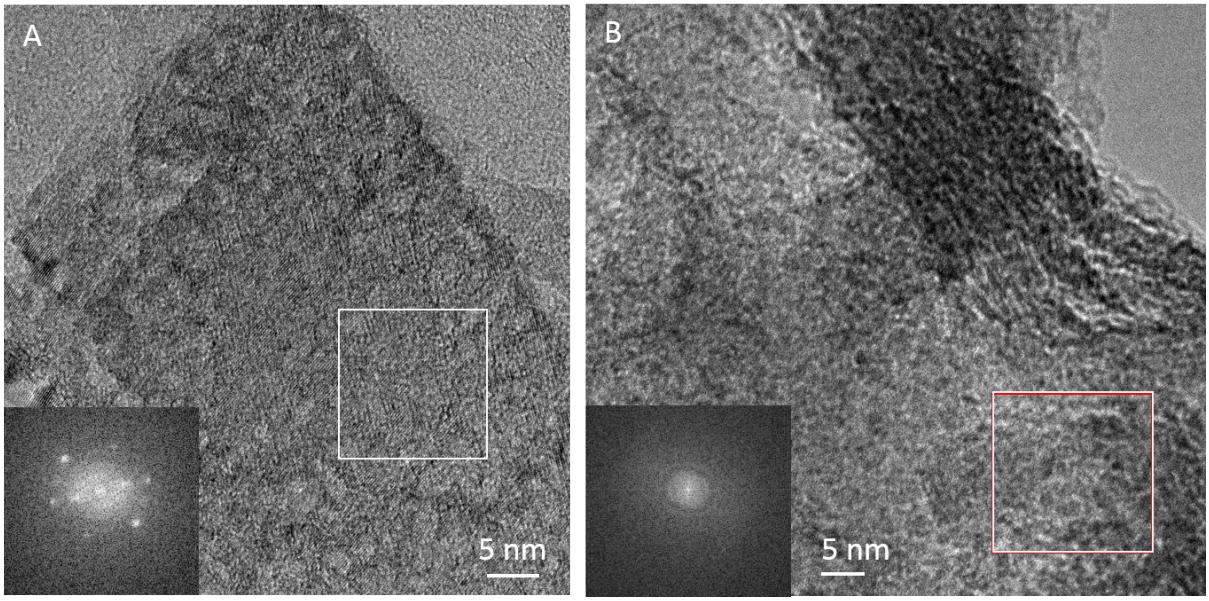

Figure S9: High resolution TEM images of liquid exfoliated $Ni(OH)_2$ nanosheets before (A) and after (B) activation. The image in A represents an as-prepared sample while the image in B represents a sample which had been activated for 100 hours and subjected to OER analysis. The sample in B was removed from the Ni foam by mild sonication (sonic bath for 1

hr). Fast Fourier transforms were collected from the regions surrounded by the white boxes and are shown as insets.

5.5 UV/Vis/nIR Absorption of $Ni(OH)_2$

The absorption spectra (Figure S7) show clear peaks associated with Ni^{2+} in $Ni(OH)_2$.The peak centred around 1100 nm is due to the $^3A_2 \rightarrow {}^3T_2(^3F)$ transition, the peak at 700 nm is the $^3A_2 \rightarrow {}^3T_1(^3F)$ and the peak at 400 nm is the $^3A_2 \rightarrow {}^3T_1(^3P)$ transition, all from Ni^{2+} in octahedral symmetry. These transitions are assigned on the basis of the d^8 system with the local crystal field altering the free ion levels. We note that all the peaks are split into two, indicating a lower local symmetry than octahedral. From the positions of these transitions, we can derive the crystal field parameters for Ni^{2+} in this hydroxide material by fitting with the Sugano-Tanabe diagrams. The energy splitting of the $^3A_2 \rightarrow {}^3T_2(^3F)$ transition is written as 10 Dq, so Dq is 910 cm^{-1}. The positions of the other two spin allowed $^3A_2 \rightarrow {}^3T_1(^3F)$, $^3A_2 \rightarrow {}^3T_1(^3P)$ transitions allow us to calculate the Dq value along with the Racah B factor, which we find to be 830 cm^{-1}. There are many other spin forbidden and weak transitions on the Ni^{2+} ion which depend on Dq, B and the parameter C also. We do not find any evidence for these weak transitions in the measured spectra and so cannot determine C. Comparing these values with the cases of oxide host materials, the Dq and B values are larger in the case of $LiGa_5O_8$[30] and MgO compared with our $Ni(OH)_2$ case. In addition, the crystal field parameters are larger than in fluoride hosts[31].

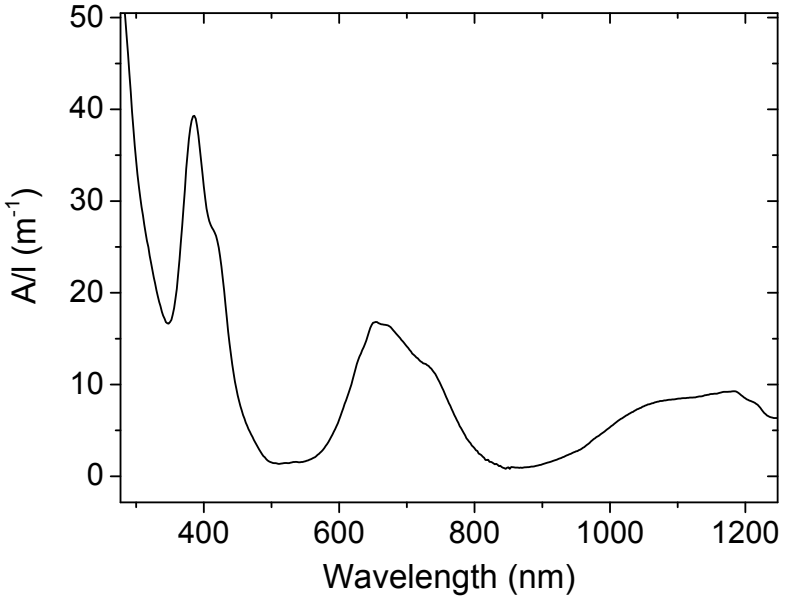

Figure S10: UV-Vis-NIR) Absorption spectra for the $Ni(OH)_2$ standard sample in H_2O/SC, t_{sonic} = 4 h, C_i = 20 g/L, C_{surf} = 9 g/L. A Perkin Elmer Lamda1050 spectrometer equipped with a 150mm integrating sphere with PMT and InGaAs detector was used for the measurement.

6. Size selection of $Ni(OH)_2$ nanosheets

All TEM length histograms along with representative images of the $Ni(OH)_2$ size selected by liquid cascade centrifugation are shown in Figure S8.

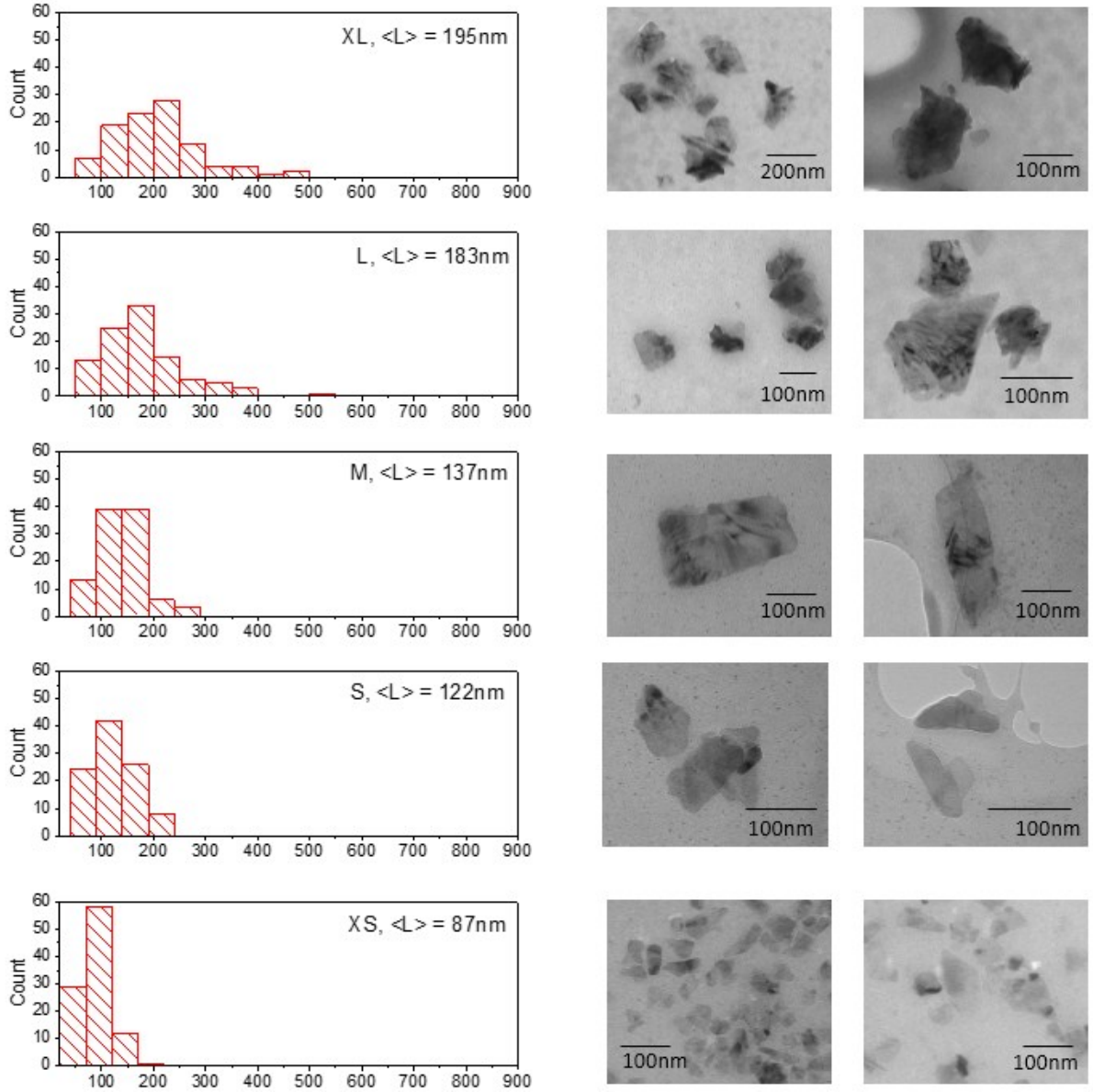

Figure S11) Length histograms of $Ni(OH)_2$ in H_2O/SC of varying sizes obtained from liquid cascade centrifugation as outlined in the methods section. The size was determined by statistical TEManalysis. Representative TEM images of each size are shown in the right panels.

7. Additional Electrochemical Characterisation

7.1 Supercapacitors

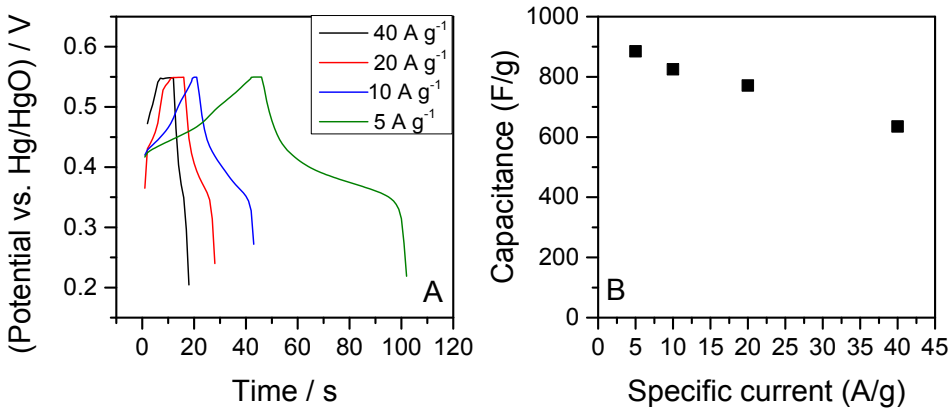

Figure S12: A) Galvanostatic charge/discharge curves for the (activated) $Ni(OH)_2$ supercapacitor electrodes described in the text. B) Data for capacitance plotted versus current. These values are very similar to the low rate values measured by cyclic voltammetry described in the text.

7.2 Impedance Analysis

A.C impedance measurements were performed on electrodes after 100 hours activation as a function of increasing overpotential into the oxygen evolution region as shown in the Bode plot below (figure S13). At the high frequency intercept, one can see that the impedance retains a constant value of *ca.* 1.5 Ω despite more vigorous gas evolution at higher potentials. Lyons and Brandon[32] note that the high frequency response is composed of the electrolyte resistance coupled with the resistance and capacitance of the film. Thus we can infer two things here: First, that the film resistance, (or conductivity), remains relatively constant with increasing potential and that the electrolyte resistance is independent of potential in the potential region studied. In addition, by examining the linear sweep curves in the main text, one can see that the transportation of the electrolyte, or more specifically the OH^- ions, are not limited by diffusion due to the lack of a mass transport limiting region being present. In addition, one would expect to see an increase in impedance with increasing potential there was significant gas shielding preventing the transport of the electrolyte to the electrode which from the fig below we do not see.

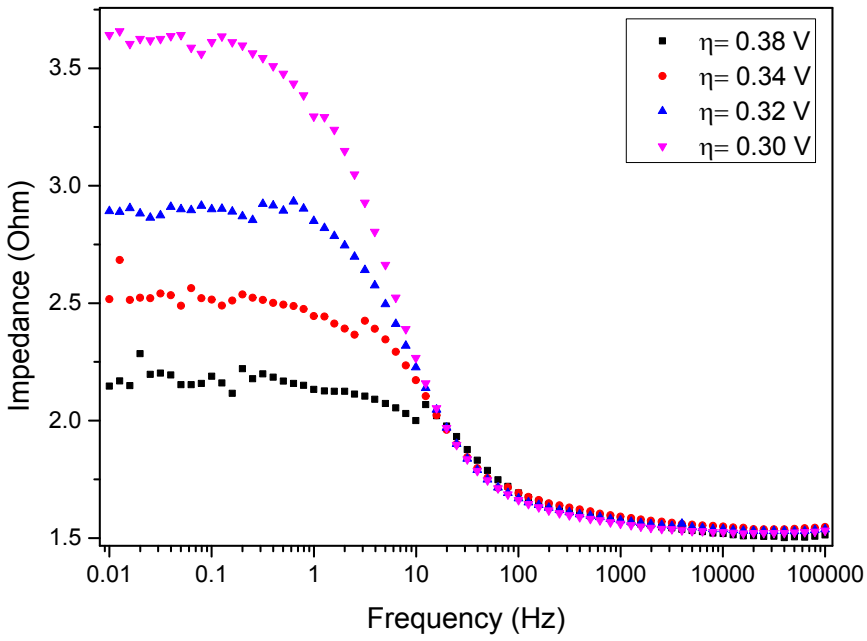

Figure S13: Impedance response of $Ni(OH)_2$ on nickel foam as a function of potential in the oxygen evolution region.

8. Supporting references

1. S. J. Ding, T. Zhu, J. S. Chen, Z. Y. Wang, C. L. Yuan and X. W. Lou, *Journal of Materials Chemistry*, 2011, 21, 6602-6606.
2. D. S. Hall, D. J. Lockwood, S. Poirier, C. Bock and B. R. MacDougall, *Acs Appl Mater Inter*, 2014, 6, 3141-3149.
3. Y. Wang, Q. Zhu and H. Zhang, *Chemical Communications (Cambridge, England)*, 2005, DOI: 10.1039/b508807k, 5231-5233.
4. J. Y. Y. H. Pirre P. Ylä-Mäihäniemi , Frank Thielmann and Daryl R. Williams *Langmuir*, 2008, 24, 9551-9557.
5. M. G. Huson, J. S. Church, A. A. Kafi, A. L. Woodhead, J. Khoo, M. S. R. N. Kiran, J. E. Bradby and B. L. Fox, *Carbon*, 2014, 68, 240-249.
6. R. Menzel, A. Bismarck and M. S. P. Shaffer, *Carbon*, 2012, 50, 3416-3421.
7. H. Balard, D. Maafa, A. Santini and J. B. Donnet, *Journal of chromatography. A*, 2008, 1198-1199, 173-180.
8. J. B. Donnet, S. J. Park and M. Brendle, *Carbon*, 1992, 30, 263-268.
9. E. Papirer, E. Brendle, F. Ozil and H. Balard, *Carbon*, 1999, 37, 1265-1274.
10. J. Donnet, S. J. Park and H. Balard, *Chromatographia*, 1991, 31, 434-440.
11. R. Ho, S. J. Hinder, J. F. Watts, S. E. Dilworth, D. R. Williams and J. Y. Heng, *Int. J. Pharm.*, 2010, 387, 79-86.
12. S. C. Das, I. Larson, D. A. Morton and P. J. Stewart, *Langmuir*, 2011, 27, 521-523.
13. R. R. Smith, D. R. Williams, D. J. Burnett and J. Y. Y. Heng, 2014.
14. G. M. Dorris and D. G. Gray, *Journal of Colloid and Interface Science*, 1980, 77, 353-362.
15. M. G. Cares-Pacheco, R. Calvet, G. Vaca-Medina, a. Rouilly and F. Espitalier, *International Journal of Pharmaceutics*, 2015, 494, 113-126.
16. J. F. Gamble, M. Leane, D. Olusanmi, M. Tobyn, E. Supuk, J. Khoo and M. Naderi, *Int. J. Pharm.*, 2012, 422, 238-244.
17. A. Ferguson, U. Khan, M. Walsh, K.-Y. Lee, A. Bismarck, M. S. P. Shaffer, J. N. Coleman and S. D. Bergin, *Biomacromolecules*, 2016, 17, 1845-1853.
18. R. Ho, M. Naderi, J. Y. Heng, D. Williams, F. Thielmann, P. Bouza, A. Keith, G. Thiele and D. Burnett, *Pharm Res*, 2012, 29, 2806-2816.
19. C. J. Van Oss, R. J. Good and M. K. Chaudhury, *Chemical Reviews*, 1988, 88, 927-941.
20. C. Volpe and S. Siboni, *Journal of colloid and interface science*, 1997, 195, 121-136.
21. C. Backes, R. J. Smith, N. McEvoy, N. C. Berner, D. McCloskey, H. C. Nerl, A. O'Neill, P. J. King, T. Higgins, D. Hanlon, N. Scheuschner, J. Maultzsch, L. Houben, G. S. Duesberg, J. F. Donegan, V. Nicolosi and J. N. Coleman, *Nature Communications*, 2014, 5, 4576.
22. C. Backes, B. M. Szydłowska, A. Harvey, S. Yuan, V. Vega-Mayoral, B. R. Davies, P.-l. Zhao, D. Hanlon, E. J. G. Santos, M. I. Katsnelson, W. J. Blau, C. Gadermaier and J. N. Coleman, *ACS Nano*, 2016, 10, 1589-1601.
23. K. R. Paton, E. Varrla, C. Backes, R. J. Smith, U. Khan, A. O'Neill, C. Boland, M. Lotya, O. M. Istrate, P. King, T. Higgins, S. Barwich, P. May, P. Puczkarski, I. Ahmed, M. Moebius, H. Pettersson, E. Long, J. Coelho, S. E. O'Brien, E. K. McGuire, B. M. Sanchez, G. S. Duesberg, N. McEvoy, T. J. Pennycook, C. Downing, A. Crossley, V. Nicolosi and J. N. Coleman, *Nature Materials*, 2014, 13, 624-630.
24. D. S. Hall, D. J. Lockwood, S. Poirier, C. Bock and B. R. MacDougall, *The Journal of Physical Chemistry A*, 2012, 116, 6771-6784.
25. A. Van der Ven, D. Morgan, Y. S. Meng and G. Ceder, *Journal of The Electrochemical Society*, 2006, 153, A210-A215.
26. M. Casas-Cabanas, J. Canales-Vázquez, J. Rodríguez-Carvajal and M. R. Palacín, *Journal of the American Chemical Society*, 2007, 129, 5840-5842.

27. A. Demourgues, L. Gautier, A. V. Chadwick and C. Delmas, *Nuclear Instruments and Methods in Physics Research Section B: Beam Interactions with Materials and Atoms*, 1997, 133, 39-44.
28. L. Liu, Z. Zhou and C. Peng, *Electrochim. Acta*, 2008, 54, 434-441.
29. N. Sac-Epée, M. R. Palacìn, A. Delahaye-Vidal, Y. Chabre and J. M. Tara⁄scon, *Journal of The Electrochemical Society*, 1998, 145, 1434-1441.
30. J. F. Donegan, T. J. Glynn, G. F. Imbusch and J. P. Remeika, *J Lumin*, 1986, 36, 93-100.
31. W. E. Vehse, K. H. Lee, S. I. Yun and W. A. Sibley, *J Lumin*, 1975, 10, 149-162.
32. M. E. G. Lyons and M. P. Brandon, *Journal of Electroanalytical Chemistry*, 2009, 631, 62-70.